Investigating Phase-Change-Induced Flow in Gas Diffusion Layers in Fuel Cells with X-ray Computed Tomography

Andrew D. Shum[1], Dilworth Y. Parkinson[2], Xianghui Xiao[4], Adam Z. Weber[3], Odne S. Burheim[5], Iryna V. Zenyuk[1,*]

[1]Department of Mechanical Engineering, Tufts University, Medford, MA 02155

[2]Advanced Light Source, [3]Energy Storage and Distributed Resources Division, Lawrence Berkeley National Laboratory, 1 Cyclotron Road, Berkleey CA 94720, USA

[4]X-ray Science Division, Argonne National Laboratory, 9700 S. Class Avenue, Lemont IL 60439, USA

[5]Dep. Of Energy and Process Engineering, NTNU – the Norwegian Univ. of Sci. and Technol., NO-7491 Trondheim, Norway

*Corresponding Author: 200 Boston Ave. 2600, Medford, MA 02155

e-mail: iryna.zenyuk@tufts.edu

Abstract

The performance of polymer-electrolyte fuel cells is heavily dependent on proper management of liquid water. One particular reason is that liquid water can collect in the gas diffusion layers (GDLs) blocking the reactant flow to the catalyst layer. This results in increased mass-transport losses. At higher temperatures, evaporation of water becomes a dominant water-removal mechanism and specifically phase-change-induced (PCI) flow is present due to thermal gradients. This study used synchrotron based micro X-ray computed tomography (CT) to

visualize and quantify the water distribution within gas diffusion layers subject to a thermal gradient. Plotting saturation as a function of through-plane distance quantitatively shows water redistribution, where water evaporates at hotter locations and condenses in colder locations. The morphology of the GDLs on the micro-scale, as well as evaporating water clusters, are resolved, indicating that the GDL voids are slightly prolate, whereas water clusters are oblate. From the mean radii of water distributions and visual inspection, it is observed that larger water clusters evaporate faster than smaller ones.

Keywords: porous media, fuel cells, phase-change-induced flow, evaporation, X-ray tomography

1. Introduction

The performance of polymer-electrolyte fuel cells (PEFCs) and other multiphase flow technologies is significantly dependent on liquid-water management [1-3]. This is particularly true for PEFCs at low operating temperatures and during startup operations due to hindered reactant delivery by water in cathode [4-8]. Because of the exothermic oxygen reduction reaction (ORR) at the cathode, a thermal gradient develops during operation in the through-plane direction, with the hottest location in the catalyst layer (CL). At higher temperatures (~80 °C), this thermal gradient, in combination with the dependence of vapor pressure on temperature, promotes removal of water in a vapor form [1, 4, 9-12]. Water vapor within the CL travels through the gas diffusion layer (GDL) to the gas channels (GCs) (see Figure 1), where it condenses due to the decrease in temperature. This type of flow, which is due to the evaporation and condensation of water, is known as phase-change-induced (PCI) flow [4, 13]. The driving force for PCI flow within the porous media of the fuel cell is the temperature gradient. Although

water is removed in the vapor phase, depending on a PEFC's operating temperature, a fraction of the total water has to still be removed in the liquid phase. Thus PEFCs experience two-phase water flow and, consequently, substantially coupled heat and mass transport. As such, effective water management requires an understanding of the interaction between pressure-driven, capillary-driven, and PCI water transport [4, 14]. Phase change is not a drive potential or force like pressure and capillary forces, however, the term "PCI" has become the common name in literature for heat-driven mass transport of water by evaporation and condensation in a temperature gradient.

Figure 1 Goes Here

The GDL is a porous fibrous component of PEFCs responsible for the transport of electrons, water byproduct, gaseous reactants, and heat [15]. It is made from carbon fibers which are assembled to form either nonwoven paper, woven cloth, or felt. With pores on the order of 10 μ m, these materials have porosities typically ranging from 65 % to 90 % and thickness around 200 – 400 μm [16, 17]. Generally, cell compression influences the GDL's structure [15] and performance during operation. Because carbon fibers are naturally hydrophilic, GDLs are typically treated with 5 – 20 % of polytetrafluoroethylene (PTFE). Due to non-uniformities in the coating, there is a mix of hydrophilic and hydrophobic pores, which causes the overall structure to possess mixed wettability [18, 19]. As with most porous media, heat and mass transport properties depend on local morphology in addition to bulk material properties.

Most scientific work concerning transport in porous media has been conducted in the fields of civil and petroleum engineering [20-24]. Although this provides a starting point, there are a number of notable differences between the systems studied in those fields and thin materials such as GDLs and CLs. It is necessary to re-examine each of the various transport mechanisms as they

pertain to engineered systems [18]. To this end, much has already been accomplished for transport mechanisms guided by capillary, convection, and gravitational forces. Non-isothermal phenomena, on the other hand, remain an area that is not well researched [1, 4, 18]. Amongst existing non-isothermal studies, most do not address multiphase flow; let alone phase change [1]. Furthermore, those that do address multiphase flow are typically simulation-based [18] due to difficulties with an experimental approach [1].

Previous studies have shown PCI flow to be a significant contributor to overall water transport within PEFCs. For instance, Weber and Newman [1], through use of one-dimensional simulations, showed that non-isothermal effects are significant when feed gas flows are or become saturated. According to their results, net evaporation/condensation accounts for only 2.6 % of overall heat generation within a fuel cell. However, the heat generated/consumed by each individually is approximately 100 times that of the net contribution. Additionally, their work shows that a thermal gradient of only a few degrees is required across the GDL to completely remove product water from the CL, with larger thermal gradients needed at lower temperatures. As noted by Kumbur and Mench [18], the GDL provides one of the largest thermal resistances in a PEFC and therefore may experience a temperature gradient in excess of 5 °C. Kim and Mench [4] conducted an experimental study of PCI flow in which they tested various membrane-GDL combinations. It was found that PCI flow does dominate net water flux at high temperatures (80 °C). Furthermore, it was shown that incomplete saturation of the porous media is key to determining whether or not PCI flow will occur.

Over the last several years, there has been a significant effort in characterizing morphology and water distribution within the pores of the GDL by using X-ray computed tomography (CT) [25-32]. Micro-CT with a resolution of 1.3 μm is well fit to non-destructively visualize

three-dimensional GDL structures and water filling of GDL pores [15, 27, 33]. Recent studies indicate that, during PEFC operation, liquid water occupies less than 50 % [34] of the GDL pore volume because of the GDL's hydrophobic treatments, and, in the absence of temperature gradients, capillary fingering is the predominant liquid-water-transport mechanism [32, 35]. Previously, X-ray CT was used to study the evaporation of water within GDLs under constant temperature. It was found that evaporation rates at water saturations higher than 10 % scale with the surface area of water and are diffusion limited [15].

In this study, a novel X-ray CT technique to explore PCI flow within a PEFC is presented. Coupled measurements of temperature, thermal gradients, and thermal conductivity are combined with visualizations of GDL morphology and water distribution. The overall results of this study contribute to the general understanding of evaporation phenomena in porous media pertaining to PEFCs.

2. Experimental

2.1. Sample Apparatus

A custom apparatus (Figure 2), was designed and fabricated to conduct the experiment at the synchrotron X-ray CT beamlines. The design aimed to control sample compression, temperature, temperature gradient, and water capillary pressure. The apparatus adheres to size restrictions for the two different X-ray CT beamlines where data was collected and achieves a balance between the needs for structural stability and an un-obstructed view of the sample. The sample sits inside a polyetheretherkeytone (PEEK) ring. Figure 2 shows a schematic of the experimental setup, its three-dimensional rendering, and photographs of the apparatus at the two synchrotron beamlines.

The upper portion of the apparatus consists of a PEEK support structure, stainless steel

compression cap, stainless steel or aluminum piston, and copper water injection tube. The piston serves as a thermal conductor and a water pathway to simultaneously heat and fill the sample with water. The compression cap allows the piston to be pressed against the sample so as to ensure proper contact. The lower portion of the apparatus consists of a PEEK support structure, stainless steel or aluminum piston, and copper water cooling coil. The lower piston serves as a thermal conductor to remove heat from the sample. With regards to the upper and lower pistons, stainless steel was used for the initial data set. However, due to the low thermal conductivity of stainless steel, aluminum was used for further experiments. See Table 1 for general specifications of the components mentioned. K-type thermocouples (product number 5TC-TT-K-30-36 from OMEGA Engineering Inc., Norwalk, Connecticut, USA) were attached to both pistons (two each) (see Figure 3c for positions) with the leads running between the side of the pistons and a small channel in the inner wall of the PEEK supports. A Ø3 mm cartridge heater (product number HT15W from Thorlabs Inc., Newton, New Jersey, USA) was concentrically inserted through the compression cap and into the top of the upper piston. Lastly, three Nylon thumb screws hold the upper support, sample ring, and lower support together.

Figure 2 Goes Here

Table 1. General specifications for apparatus parts. Some dimensions have been converted from US customary units.

Part	Material	General Dimensions
sample ring	PEEK	5 OD × 4 ID × 2 mm
upper support	PEEK	main: Ø40 × 45 mm flange: Ø50.8 × 4 mm lip: 5 OD × 4 ID × 1 mm
lower support	PEEK	main: Ø40 × 45 mm flange: Ø50.8 × 5 mm
upper piston	304 stainless steel 6061 aluminum	Ø4 × 40 mm
lower piston	304 stainless steel 6061 aluminum	upper: Ø4 × 50.5 mm lower: Ø25.4 × 51.1 mm
cooling coil	copper	tube: 6.4 OD × 3.9 ID mm coil: 25.4 mm ID, 6.4 mm pitch, 4.5 turns
water injection tube	copper	3.2 OD × 1.5 ID × 76.2 mm
compression cap	304 stainless steel	overall: 10 OD × 3.2 ID × 30 mm threaded bottom: M10×1.5 × 15 mm
thumb screws	Nylon	#6-32 × 1 in. (cut to length)

2.2. Beamlines

X-ray tomographic microscopy imaging was conducted at two different beamlines. The first set of experiments was carried out at Beamline 8.3.2 of the Advanced Light Source (ALS) at Lawrence Berkeley National Laboratory (LBNL), Berkeley, CA, USA. A second set of this experiment was conducted at Beamline 2-BM-A of the Advanced Photon Source (APS) at Argonne National Laboratory (ANL), Lemont, IL, USA.

2.2.1. ALS

Image acquisition was conducted using a 500 μm LuAG scintillator, 5x lenses, and a sCMOS PCO. Dimax camera. This resulted in 2.2 μm cubic voxels and a horizontal field of view (FOV) of 4.4 mm. A double-multilayer monochromator was used to select a beam energy of 22 keV. Each scan was performed over a rotation range of 180° with 1025 projections and an exposure

time of 40 ms.

2.2.2. APS

Image acquisition was conducted using a 20 μm LuAG scintillator, 5x lenses, and a sCMOS PCO. Edge camera. This resulted in 1.33 μm cubic voxels and a horizontal FOV of 3.3 mm. A double-multilayer monochromator was used to select a beam energy of 25 keV. Each scan was performed over a rotation range of 180° with 1500 projections, an exposure time of 50 ms, and a total scan time of 3 minutes.

2.3. Materials and Setup

SGL10BA (SGL CARBON GmbH - Fuel Cell Components, Meitingen, Germany) was used as the GDL sample in this study. This sample was chosen because it was previously well studied with X-ray CT [15, 32] and is easy to handle. In order to obtain a larger thermal gradient, the sample consisted of a stack of two GDLs. Water capillary pressure was controlled by attaching a flexible tube to the water injection tube and then adjusting the water column height to 2 – 3 cm. After water injection and before each tomography scan, temperatures and heat flux were recorded. The scans were timed to have these measurements every 13 minutes. For each heat flux, 4 – 5 measurements and scans were done; after which the heat flux was increased by stepping the voltage to the heater by 1 V on the power supply. Data collection for a given case was stopped when water completely evaporated within the GDL (as observed with X-ray CT scans). Each case lasted 50 – 200 minutes. Cooling was accomplished by using flexible tubing to connect the cooling coil to a refrigerated water bath. Temperature data was obtained through use of a thermocouple data acquisition board (product number IPDAS TC from CyberResearch Inc.,

Branford, Connecticut, USA). Temperature drops across the apparatus ranging from 15 °C to 28 °C were generated by adjusting the voltage applied to the resistive heater. The setup was insulated resulting in negligible heat escape through the top and sides of the PEEK, ensuring one-dimensional heat transport through the sample.

2.4. Image Processing

2.4.1. Data Reconstruction

For data from ALS, preprocessing was conducting using Fiji/ImageJ [36]. This was followed by the Modified Bronnikov Algorithm (MBA) to retrieve phases and reconstruction using Octopus 8.6 [37]. For APS data, all steps of reconstruction were conducted using the TomoPy package (version 0.1.15) for Anaconda/Python. First the sinograms were normalized to the white and dark field projections. Then they were normalized to the background intensity using a scaling factor based on 10 pixels from the right boundary and another 10 pixels from the left boundary. Horizontal stripes were removed using the sym16 wavelet filter with 10 discrete wavelet transform levels and a Fourier space damping parameter of 1. For the actual reconstruction, the Gridrec algorithm was applied [38].

2.4.2. Segmentation and Results Collection

Post reconstruction processing was conducted using Fiji/ImageJ [36]. All images were cropped to include the region of interest but exclude the significant reconstruction artifacts along the edges. Separation of three phases (voids, fibers, and water) was obtained through use of a dry reference image for each sample. For these reference images, voids and fibers were separated using the Otsu algorithm. For images of saturated samples, manual threshold determination was

used to separate voids from fibers and water. The corresponding reference image was then subtracted from the sample image to isolate water. Next, ImageJ's "Open" operation (erosion followed by dilation) was used to remove noise from the images of the isolated phases. The operation was repeated 8 times for ALS data and 6 times for APS data (these were the optimum parameters). In both cases, the minimum neighbor count was 4.

Through-plane porosity was determined by counting the number of background pixels in the reference image. This was done separately for each slice; thus corresponding to depth into the GDL. Through-plane water volume fraction was determined in a similar manner but using the isolated water images. The through-plane saturation was then calculated from the porosity and water content data. Both pore size distributions and water cluster size distributions were determined using the Local Thickness plug-in [39]. Local Thickness utilizes sphere fitting and assigns a pixel value equal to the radius of the largest sphere whose domain contains the pixel. Classification of pore/water cluster shape was conducted using the ellipsoid factor (EF) method [40] from the BoneJ plug-in [41]. The EF method utilizes ellipsoid fitting to calculate an index (see "Supplemental Information" section 3.3 for details; Figure S5 provides example ellipsoids) used to classify pores/clusters according to shape.

3. Calculations

3.1. Thermal Conductivity

Assuming one-dimensional heat flow though the setup, heat flux and temperature are coupled by the following formulation of Fourier's Law.

$$q = -k\frac{\Delta T}{\Delta x} \tag{1}$$

where q is heat flux per unit area, k is thermal conductivity, ΔT is temperature difference, and Δx is position difference. Thermal resistance, R [K W^{-1}], can be used to rearrange Equation (1) as follows were Q is heat flux and A is cross-sectional area:

$$\Delta T = -QR \tag{2}$$

$$R = \frac{\Delta x}{kA} = -\frac{\Delta T}{Q} \tag{3}$$

Figure 3 Goes Here

Figure 3c shows relevant temperature locations. Taking T_3/T_4 to be at 0 mm along their respective pistons, T_2/T_5 are at 5 mm and T_1/T_6 are at 15 mm. T_6 is at 10 mm for the lower steel piston. T_1, T_2, T_5, and T_6 correspond to thermocouple readings while T_3 and T_4 correspond to extrapolated temperatures. Using the thermal resistance network in Figure 3a, the following equation can be derived where R_{tot} is the resistance calculated using T_{top} and T_{bot}, the temperatures at the tips of the top and bottom pistons respectively. Note that $R_{cont,\,top}$, R_{samp}, $R_{cont,\,bot}$, and R_{PEEK} are the thermal resistances of contact at the top of the sample, the sample itself, contact at the bottom of the sample, and the sample ring respectively.

$$\frac{1}{R_{tot}} = \frac{1}{R_{cont,top} + R_{samp} + R_{cont,bot}} + \frac{1}{R_{PEEK}} \tag{4}$$

$$R_{samp} = \frac{1}{\frac{1}{R_{tot}} - \frac{1}{R_{PEEK}}} - R_{cont,top} - R_{cont,bot} \quad (5)$$

Combining Equation (3) and Equation (5, Equation (6 can be derived and solved for the GDL thermal conductivity:

$$\frac{\Delta x_{samp}}{k_{samp} A_{samp}} = \frac{1}{\frac{Q_{tot}}{T_{top} - T_{bot}} - \frac{k_{PEEK} A_{PEEK}}{\Delta x_{PEEK}}} - R_{cont,top} - R_{cont,bot} \quad (6)$$

$$k_{samp} = \frac{\Delta x_{samp}}{A_{samp}\left(\frac{1}{\frac{Q_{tot}}{T_{top} - T_{bot}} - \frac{k_{PEEK} A_{PEEK}}{\Delta x_{PEEK}}} - R_{cont,top} - R_{cont,bot}\right)} \quad (7)$$

where Δx_{samp} is sample thickness, k_{samp} is sample thermal conductivity, A_{samp} is GDL cross-sectional area, Q_{tot} is total heat flux through the apparatus, Δx_{PEEK} is the PEEK ring thickness (approximately same as GDL thickness), k_{PEEK} is the thermal conductivity of PEEK, and A_{PEEK} is the cross-sectional area of the PEEK ring. By assuming no significant inductive or capacitive effects, use of a resistive heater allows for the following equation to be used. R_{heater} is the resistance of the heater and V_{heater} is the voltage across the heater's leads.

$$Q_{tot} = \frac{V_{heater}^2}{R_{heater}} \quad (8)$$

The contact resistances are estimated using data from [42] along with the following equation:

$$R_{cont} = \frac{r_{cont}}{A_{cont}} \tag{9}$$

where r_{cont} is the value as provided by [42] and A_{cont} is the simple geometric area of the contact surface. The thermal conductivity of the sample can then be determined by applying Equation (7), Equation (8), and Equation (9) using the data summarized in Table 2.

Table 2. Values used to compute thermal conductivity of the GDL.

Parameter	Value	Units	Method of Acquisition
Δx_{samp}	482.6	μm	Average calculated using visual selection of surfaces in tomogram
A_{samp}	12.57	mm^2	Assumed same as $A_{cont, bot}$
V_{heater}	Various	V	Power supply readout
R_{heater}	38.4	Ω	Average calculated using power supply current and voltage readouts
T_{top}	Various	°C	Linear extrapolation along heated piston
T_{bot}	Various	°C	Linear extrapolation along cooled piston
k_{PEEK}	0.25	$W\ m^{-1}\ K^{-1}$	Common value provided by multiple suppliers
A_{PEEK}	7.1	mm^2	Calculated from caliper measurements of inner and outer diameters
Δx_{PEEK}	482.6	μm	Assumed same as Δx_{samp}
$r_{cont, top}$	7.2×10^{-4}	$m^2\ K\ W^{-1}$	From data in [42]
$A_{cont, top}$	12.57	mm^2	Estimated same as $A_{cont, bot}$
$r_{cont, bot}$	0.45×10^{-4}	$m^2\ K\ W^{-1}$	Linearly extrapolated from data in [42]
$A_{cont, bot}$	12.57	mm^2	Calculated from design diameter

3.2. Water Vapor Flux

In order to compare results to previous literature, it is necessary to first define tortuosity, τ. This study uses the definition put forth in [43]:

$$\tau = \frac{L_e}{L} \tag{10}$$

where L_e is the diffusion path length and L is the Euclidean distance of the diffusion path. Corresponding to this definition of tortuosity, effective diffusivity, D_{eff}, is defined as:

$$D_{eff} = \frac{\varepsilon D}{\tau^2} \tag{11}$$

where D is diffusivity and ε is porosity [43]. The water vapor flux, J, is calculated using:

$$\mathrm{J} = -\frac{D_{eff}}{R_s} \frac{d\left(\frac{P_{sat}}{T}\right)}{dT} \nabla T \tag{12}$$

from [4] where R_s is the specific gas constant of water, P_{sat} is saturation pressure, and T is temperature in Kelvin. [4] also provides a means of calculating diffusivity:

$$D = D_o \left(\frac{T}{T_o}\right)^n \frac{P_o}{P} \tag{13}$$

where D_o is diffusivity at reference absolute temperature, T_o, and reference pressure, P_o; n is a fitting parameter; and P is pressure. By combining Equation (11), Equation (12), and Equation (13); maintaining the assumption of one-dimensional heat flow; and discretizing differentials, water vapor flux can be expressed as:

$$J = -\frac{MD_o\varepsilon P_o}{R_u\tau^2 P}\left(\frac{T}{T_o}\right)^n \frac{\left(\frac{P_{sat,air,top}}{T_{top}} - \frac{P_{sat,air,bot}}{T_{bot}}\right)}{\Delta x_{samp}} \quad (14)$$

where M is the molar mass of water, R_u is the universal gas constant, $P_{sat,air,top}$ and $P_{sat,air,bot}$ are saturation pressures in air at the top and bottom of the sample respectively, and temperatures are in Kelvin. According to [44], saturation pressure, over the temperature range of 0 °C to 100 °C, is given by:

$$P_{sat,air} = fP_{sat,vap} \approx P_{sat,vap} = 611.21e^{\frac{17.123T}{T+234.95}} \quad (15)$$

where f is the enhancement factor (~1), $P_{sat,vap}$ is saturation pressure in water vapor, and temperature is in Celsius.

Table 3. Values used to predict water vapor flux.

Parameter	Value	Units	Source
D_o	$2.26 \cdot 10^{-5}$	$m^2\ s^{-1}$	[4]
P_o	1	bar	[4]
P	1	bar	assumed
T	$0.5 \cdot (T_{top} + T_{bot})$	K	experiment data
T_o	273.15	K	[4]
n	1.81	-	[4]
$\tau^2 \cdot \varepsilon^{-1}$	1.5	-	[4]
τ^2	1.5	-	[15]
ε_1	0.84	-	[15]
ε_2	Various	-	experiment data

4. Results and Discussion

4.1. Thermal Considerations

Figure 4 shows mean temperature of the GDL, temperature drop across it, and calculated thermal conductivity as a function of heat flux. Per each heat flux value, multiple measurements are shown. These are measurements for different times as plotted by Figure 5. Figure 4a-b clearly show the same trends observed in Figure 5a-b. However, Figure 4c shows a gradual decrease in thermal conductivity with increasing heat flux. At higher heat flux values, liquid water saturation decreases until complete dryout; thus, at lower heat flux values, there is a higher content of liquid water in the sample. Since water's thermal conductivity is about 20 times higher than that of air, net thermal conductivity is slightly higher at low heat flux values due to increased saturation. This observation is consistent with previous studies where higher thermal conductivities were observed for saturated samples due to water having a higher thermal conductivity than air and providing better fiber to fiber connectivity [45]. The reason such a small decrease in thermal conductivity was observed in this study is that, at all points, saturation levels were relatively low (< 0.2 compared to $0.4 – 0.7$).

Figure 4 Goes Here

Figure 5a shows the hot, cold, and mean temperatures as a function of time with dashed lines indicating a point in time for water injection. This plot also shows a gradual increase in the mean temperature with time. Different symbols correspond to various heat fluxes, as shown in Figure 4. While the increase can be attributed to increases in heat flux, Figure 4a shows that this occurs even when the heat flux is kept constant. The simplest explanation for this is that the system is in a pseudo-steady state. Figure 5b shows the temperature drop over the sample. The temperature drop remains relatively constant, around 8 °C. Unlike the mean temperature, the temperature drop for a given heat flux fluctuates. More specifically, the time data (Figure 5b) shows that the

temperature drop tends to increase and then decrease with time for a given heat flux. At first, this seems like random fluctuations. Further consideration presents the possibility that this may be the combined result of a thermal "response time" and evaporation/condensation. Figure 5c shows near-zero saturation approaching the moment of water injection. Since evaporation/condensation is the proposed mechanism of heat transport, it is reasonable to assume that low saturation would hinder heat transport and thus prevent equalization of the sample's face temperatures. Consistent with this proposed mechanism, the injection of water at 187 minutes corresponds to a significant increase in saturation (Figure 5c) and the onset of decreasing temperature drop (Figure 5b). As such, this behavior appears to verify the importance of PCI flow.

Overall saturation (Figure 5c) does not experience a substantial decrease until a time of 143 minutes. The first two measurement points were collected as the system was equilibrating and were excluded from the analysis. The particular scan at which evaporation appears to dramatically increase corresponds to a mean temperature of 49 °C and a temperature drop of 7.4 °C. This point divides the apparent regimes of slow and fast evaporation, which is discussed in detail in section 4.4 of this manuscript. After the second injection of water at 173 minutes, the dryout of the GDL occurred within 50 minutes. This was because a high heat flux of 225 kW m^{-2} was supplied; causing high evaporation rates. The "slow" evaporation regime persisted for only 30 minutes compared to more than 100 minutes for the first water injection where lower heat fluxes were applied. Thermal conductivity remains approximately constant at 0.68 W m^{-1} K^{-1} (about two times that of the dry GDL [42]) as shown by Figure 5d, with an observed small decrease with lower saturations.

Figure 5 Goes Here

4.2. Through-plane Saturation

Figure 6 shows the through-plane saturation and GDL porosity corresponding to representative data points from 53 to 157 minutes in Figure 5; where 0 μm is the top piston (hot location). The water distribution at time 53 is equilibrated water distribution after liquid water injection. Figure 6a clearly shows a decrease in saturation with time in all GDL locations, particularly near the hot piston, until complete dryout at time of 157 minutes. Figure 6b shows each saturation data set normalized to its own volume average. Essentially, this adjusts each data set such that they may be compared as if taken at the same overall saturation, *i.e.*, the liquid-water content remains unchanged for all heat flux and time series. If liquid-water content stays the same within the enclosed volume, it can only spatially change and redistribute. This water redistribution is clearly seen in Figure 6b where significant evaporation and a decrease in saturation is observed with time at the GDL's hot side and condensation of water is observed 305 μm into the GDL, close to the cold piston. The saturation in the middle of the GDL remains unchanged. This behavior is consistent with what would be expected from PCI flow.

Figure 6 Goes Here

4.3. Evaporation of Water Clusters

Figure 7 shows volume-rendered images of the GDLs corresponding to the data in Figure 6. These images aid in visualizing the changes described by numeric data. The time sequence is described from the left (t = 53) to the right (t = 157). The dramatic change between the last two time steps corresponds to the "rapid" evaporation shown in Figure 5c. The shift towards smaller water clusters, as will be explained by Figure 8a, is also noticeable. Furthermore, looking at the gray-scale cross-section tomographs of the GDL near the hot location (Figure 7c), fast evaporation, primarily that of large water domains, is observed. From the cross-section

tomographs near the cold location of the GDL (Figure 7d), water redistribution is observed with almost no evaporation in the first three images and complete dryout in the last image.

Figure 7 Goes Here

Through-plane saturation data is useful for determining the amount of water present. However, it does not provide any insight with regards to cluster geometry. For this, it is desirable to know both the size and the shape of the water clusters as well as compare the cluster geometry to that of the pores. Precisely defining the geometry of each pore/cluster is unrealistic and does not add much value. As such, sphere and ellipsoid fitting (described in "Supplemental Information" section 3.3) may be used to group clusters by similar geometric properties. The collection of these groups can then be represented as a discrete probability density function (PDF) relative to the total pore/cluster volume. Figure 8 shows the size and EF distributions corresponding to the data in Figure 6 (see Figure S4 for PDFs as functions of both size and EF). Plotting the distributions with respect to time visually demonstrates the impact of evaporation. As seen from the size distributions, the water clusters start with a distribution similar to that of the pores. However, as evaporation occurs, water distributions shift towards smaller cluster sizes. Also note that the initial size distribution is already biased towards smaller clusters. For radii smaller than 20 μm, water clusters favor the smallest size possible while pores have peak radii around 10 μm and no observable peak at a lower radius. Although this is visible in Figure 8a, it is more clearly shown in Figure S3c. During evaporation, this preference for forming the smallest clusters possible persists in addition to an overall distribution shift towards smaller radii (from 19.9 μm to 14.5 μm at 0 minutes and 90 minutes, respectively). This is consistent with what one would expect due to the mixed-wettability nature of the GDL; water evaporates from larger pores first and condenses into smaller pores.

For cluster shape, the EF distributions show a preference for negative EF values. This corresponds to oblate water clusters. In contrast, the pore shapes show a preference for prolate ellipsoids. In either case, the mean EF values are close to zero. A trend worth noting is that the magnitude of the mean EF values for water clusters decrease with time (evaporation). This indicates that water cluster shapes become less oblate as evaporation occurs, even though the slight tendency towards oblate shapes remains.

Figure 8 Goes Here

4.4. Regional Saturation and Local Evaporation

Figure 9 divides the GDL into 3 regions equally spaced in the through-plane direction (top, middle, and bottom) with dashed lines indicating when additional water was injected. From the average saturation data (Figure 9a), it can be seen that the top (hot) region of the GDL contains noticeably less water than the middle and bottom (cold) regions. Another interesting trend occurs prior to the significant decrease in saturation. In the time between 53 minutes and 143 minutes, which is the "slow" evaporation regime, the top experiences the highest evaporation rate while the bottom experiences the lowest evaporation rate. This is due to the fact that the top is at a higher temperature than the bottom of the GDL and confirms the PCI-flow observation. Figure 9b shows that the behavior of the mean water cluster radius is similar to that of the average saturation. This is what one would expect given that Figure 6a shows a decrease in saturation with time and Figure 8a shows a decrease in mean pore radius with time.

Figure 9 Goes Here

The saturation data in Figure 9a shows the same type of behavior as the overall saturation data (Figure 5c); primarily, there is a sudden increase in the saturation reduction rate at 143 minutes. As mentioned while discussing Figure 5c, this suggests two regimes of evaporation.

However, identifying the first regime (53 minutes to 143 minutes) as the slow regime is actually incorrect. To understand why, it is important to refer back to the experimental setup. Recall that additional tubing was attached to the water injection tube. This additional tubing was then filled with water to achieve a specific water column height and, in doing so, control capillary pressure. Also, the tomographic scans were taken at each heat flux until the water in the GDL was completely evaporated. This, as observations confirm, means that the entire contents of the water column has also been evaporated as it entered the GDL. The reason is that, while water in the GDL is evaporated, the water column provides a reservoir from which replacement liquid water is taken. Therefore, two regimes do exist; one in which evaporated water is replaced due to the reservoir and another in which it is not because the reservoir has been depleted. These two cases are depicted in Figure 9c-d respectively. Since liquid water is replaced during the first regime, this decouples the evaporation and saturation reduction rates. In order to determine the evaporation rate, the rates of saturation reduction and reduction in water column height must be combined. Table 4 shows the calculated evaporation rates assuming that the water column becomes depleted at 143 minutes. From this data, the first regime is the one that experiences a higher (2 orders of magnitude) evaporation rate. This is due to large saturation and evaporating surface area of water, as well as a substantial amount of water in contact with the hot piston, thus evaporating at faster rates. Lower evaporation rates in the second regime are due to much lower saturation values and evaporating surface areas of water; moreover at these low saturations water is in contact primarily with the cold piston.

Table 4. Evaporation rates for time spans with and without a reservoir of water for the whole GDL.

15 mm Resevoir 10^{-3} kg m^{-2} s^{-1}	30 mm Resevoir 10^{-3} kg m^{-2} s^{-1}	No Resevoir 10^{-3} kg m^{-2} s^{-1}
2.53	3.68	0.0215

Given that liquid water is produced during PEFC operation, and at constant current density is injected into the GDL, the first evaporation regime is an accurate reflection of operating conditions. However, the second regime can be applicable during the cell purge at shutdown, where irreducible water saturation needs to be removed from the cell. Figure 10 shows the evaporation rates predicted by Equation (14) using the experimental temperature values. The results are on the same order of magnitude as those predicted by the previous study, where the authors used full fuel cell hardware and a theoretical model [4]. Small variations in water flux are observed with varied values of tortuosity.

Figure 10 Goes Here

5. Conclusion

X-ray computed tomography (CT) and a custom sample apparatus were used to examine phase-change-induced (PCI) flow within SGL10BA. A thermal gradient was imposed on the stack of two GDLs and water was injected to emulate the operating conditions within a polymer-electrolyte fuel cell (PEFC). Once a pseudo-steady thermal state was reached, the sample was scanned 4 – 5 times per heat flux chosen to collect the necessary tomographic data. Tomographic scans were conducted at several heat flux values with the intent of subjecting the sample to various mean temperatures and temperature gradients.

Because data was collected while the system was in a pseudo-steady thermal state, there is a continuous gradual increase in mean temperature even when the applied heat flux does not change. The temperature drop across the stack of two GDL samples was 8 °C. The apparent

thermal conductivity of the GDL increased slightly with decreasing saturation. Error calculations (see "Supplemental Information" section 2.2) show that the most significant source of error is the uncertainty in the contact resistivities between the metal pistons and the sample.

From area-averaged saturation plots in the through-plane GDL direction, it is evident that water near the top of the GDL (hot location) evaporates at a faster rate compared to water at the bottom of the GDL (cold location). Consideration of water cluster size and shape reveal how the geometry of the water clusters change during evaporation. The initial water size distribution closely follows that of the pore size distribution. As time progresses and more water clusters evaporate, the mean radius of the water clusters decreases from 19.9 μm to 14.5 μm; more than 5 μm. Furthermore, a large peak in water distribution is observed for very small water cluster sizes. From the ellipsoid factor (EF) data, voids have a slight tendency to be prolate while water clusters have oblate shapes.

The saturation data for the sample as a whole shows a point at which a dramatic increase in the saturation reduction rate occurs. This suggests that there are two regimes of evaporative water transport. The first regime actually experiences a higher evaporation rate even if saturation decrease is slow. This is due to the presence of a water reservoir during the first regime. Because water is produced during PEFC operation, it is expected that this first regime reflects operating PEFC conditions. Net water vapor flux per kg of water was calculated and it agrees well with previous experimental studies. The follow-up study will explore PCI flow under a larger window of temperatures and temperature gradients and with various GDLs.

6. Symbols

Symbol	Explanation, Units
q''	heat flux [W m^{-2}]
k	thermal conductivity [W m^{-1} K^{-1}]
ΔT	temperature difference [K]
Δx	position difference [m]
Q	heat [W]
R	thermal resistance [K W^{-1}]
	electrical resistance [Ω]
A	cross-sectional area [m^2]
T	temperature [K]
V	direct current voltage [V]
r	thermal resistivity [m^2 K W^{-1}]
τ	tortuosity [-]
L_e	diffusion path length [m]
L	Euclidean diffusion path length [m]
D	diffusivity [m^2 s^{-1}]
ε	porosity [-]
J	water vapor flux [kg m^{-2} s^{-1}]
R_s	specific gas constant [J kg^{-1} K^{-1}]
P	pressure [Pa]
n	fitting parameter [-]
R_u	universal gas constant [J mol^{-1} K^{-1}]
M	molar mass of water [kg mol^{-1}]
f	enhancement factor [-]

7. Acknowledgements

The authors would like to acknowledge support from the National Science Foundation under CBET Award 1605159. The Advanced Light Source is supported by the Director, Office of Science, Office of Basic Energy Sciences, of the U.S. Department of Energy under Contract No. DE-AC02-05CH11231. This research used resources of the Advanced Photon Source, a U.S. Department of Energy (DOE) Office of Science User Facility operated for the DOE Office of Science by Argonne National Laboratory under Contract No. DE-AC02-06CH11357. AZW acknowledges funding under the Fuel Cell Performance and Durability Consortium (FC-PAD), by the Fuel Cell Technologies Office (FCTO), Office of Energy Efficiency and Renewable

Energy (EERE), of the U.S. Department of Energy under contract number DE-AC02-05CH11231.

References

[1] A.Z. Weber, J. Newman, Coupled Thermal and Water Management in Polymer Electrolyte Fuel Cells, Journal of The Electrochemical Society, 153 (2006) A2205.
[2] A.Z. Weber, R.L. Borup, R.M. Darling, P.K. Das, T.J. Dursch, W. Gu, D. Harvey, A. Kusoglu, S. Litster, M.M. Mench, R. Mukundan, J.P. Owejan, J.G. Pharoah, M. Secanell, I.V. Zenyuk, A Critical Review of Modeling Transport Phenomena in Polymer-Electrolyte Fuel Cells, Journal of The Electrochemical Society, 161 (2014) F1254-F1299.
[3] K.E. Ayers, J.N. Renner, N. Danilovic, J.X. Wang, Y. Zhang, R. Maric, H. Yu, Pathways to ultra-low platinum group metal catalyst loading in proton exchange membrane electrolyzers, Catalysis Today, 262 (2016) 121-132.
[4] S. Kim, M.M. Mench, Investigation of Temperature-Driven Water Transport in Polymer Electrolyte Fuel Cell: Phase-Change-Induced Flow, Journal of The Electrochemical Society, 156 (2009) B353-B362.
[5] V. Mehta, J.S. Cooper, Review and analysis of PEM fuel cell design and manufacturing, Journal of Power Sources, 114 (2003) 32-53.
[6] Y. Wang, K.S. Chen, J. Mishler, S.C. Cho, X.C. Adroher, A review of polymer electrolyte membrane fuel cells: Technology, applications, and needs on fundamental research, Applied Energy, 88 (2011) 981-1007.
[7] I.V. Zenyuk, P.K. Das, A.Z. Weber, Understanding Impacts of Catalyst-Layer Thickness on Fuel-Cell Performance via Mathematical Modeling, J Electrochem Soc, 163 (2016) F691-F703.
[8] I.V. Zenyuk, R. Taspinar, A.R. Kalidindi, E.C. Kumbur, S. Litster, Computational and Experimental Analysis of Water Transport at Component Interfaces in Polymer Electrolyte Fuel Cells, Journal of The Electrochemical Society, 161 (2014) F3091-F3103.
[9] A.Z. Weber, Fuel Cell Fundamentals at Low and Subzero Temperatures, 2014 DOE Hydrogen Program Annual Merit Reviews

2014.
[10] K.T. Cho, M.M. Mench, Fundamental characterization of evaporative water removal from fuel cell diffusion media, Journal of Power Sources, 195 (2010) 3858-3869.
[11] K.T. Cho, M.M. Mench, Effect of material properties on evaporative water removal from polymer electrolyte fuel cell diffusion media, Journal of Power Sources, 195 (2010) 6748-6757.
[12] S. Kim, M.M. Mench, Investigation of temperature-driven water transport in polymer electrolyte fuel cell: Thermo-osmosis in membranes, Journal of Membrane Science, 328 (2009) 113-120.
[13] A.Z. Weber, M.A. Hickner, Modeling and high-resolution-imaging studies of water-content profiles in a polymer-electrolyte-fuel-cell membrane-electrode assembly, Electrochimica Acta, 53 (2008) 7668-7674.
[14] Y. Wang, C.-Y. Wang, A Nonisothermal, Two-Phase Model for Polymer Electrolyte Fuel Cells, Journal of The Electrochemical Society, 153 (2006) A1193-A1200.
[15] I.V. Zenyuk, D.Y. Parkinson, L.G. Connolly, A.Z. Weber, Gas-diffusion-layer structural properties under compression via X-ray tomography, Journal of Power Sources, 328 (2016) 364-376.
[16] P.K. Sinha, P.P. Mukherjee, C.-Y. Wang, Impact of GDL structure and wettability on water management in polymer electrolyte fuel cells, Journal of Materials Chemistry, 17 (2007) 3089-3103.
[17] R.R. Rashapov, J. Unno, J.T. Gostick, Characterization of PEMFC Gas Diffusion Layer Porosity, Journal of The Electrochemical Society, 162 (2015) F603-F612.

[18] E.C. Kumbur, M.M. Mench, FUEL CELLS – PROTON-EXCHANGE MEMBRANE FUEL CELLS | Water Management A2 - Garche, Jürgen, Encyclopedia of Electrochemical Power Sources, Elsevier, Amsterdam, 2009, pp. 828-847.
[19] J.T. Gostick, M.A. Ioannidis, M.W. Fowler, M.D. Pritzker, Characterization of the Capillary Properties of Gas Diffusion Media, in: C.-Y. Wang, U. Pasaogullari (Eds.) Modeling and Diagnostics of Polymer Electrolyte Fuel Cells, Springer New York, New York, NY, 2010, pp. 225-254.
[20] M. Icardi, G. Boccardo, D.L. Marchisio, T. Tosco, R. Sethi, Pore-scale simulation of fluid flow and solute dispersion in three-dimensional porous media, Physical Review E, 90 (2014) 013032.
[21] A.Q. Raeini, B. Bijeljic, M.J. Blunt, Modelling capillary trapping using finite-volume simulation of two-phase flow directly on micro-CT images, Advances in Water Resources, 83 (2015) 102-110.
[22] A.Q. Raeini, M.J. Blunt, B. Bijeljic, Direct simulations of two-phase flow on micro-CT images of porous media and upscaling of pore-scale forces, Advances in Water Resources, 74 (2014) 116-126.
[23] Y. Zaretskiy, S. Geiger, K. Sorbie, M. Förster, Efficient flow and transport simulations in reconstructed 3D pore geometries, Advances in Water Resources, 33 (2010) 1508-1516.
[24] Y. Mehmani, M.T. Balhoff, Mesoscale and hybrid models of fluid flow and solute transport, Reviews in Mineralogy and Geochemistry, 2015, pp. 433-459.

Properties of Gas Diffusion Layers: Experiments and Simulations Using Phase Contrast Tomographic Microscopy, Journal of The Electrochemical Society, 156 (2009) B1175.
[26] F.N. Buechi, R. Flückiger, D. Tehlar, F. Marone, M. Stampanoni, Determination of Liquid Water Distribution in Porous Transport Layers, ECS Transactions, 16 (2008) 587-592.

-Ray
Tomographic Microscopy of Liquid Water in Gas Diffusion Layers of PEFC, Journal of The Electrochemical Society, 158 (2011) B963.
[28] T. Rosen, J. Eller, J. Kang, N.I. Prasianakis, J. Mantzaras, F.N. Buchi, Saturation Dependent Effective Transport Properties of PEFC Gas Diffusion Layers, Journal of The Electrochemical Society, 159 (2012) F536-F544.
[29] C. Hartnig, I. Manke, R. Kuhn, N. Kardjilov, J. Banhart, W. Lehnert, Cross-sectional insight in the water evolution and transport in polymer electrolyte fuel cells, Applied Physics Letters, 92 (2008) 134106.
[30] P. Krüger, H. Markötter, J. Haußmann, M. Klages, T. Arlt, J. Banhart, C. Hartnig, I. Manke, J. Scholta, Synchrotron X-ray tomography for investigations of water distribution in polymer electrolyte membrane fuel cells, Journal of Power Sources, 196 (2011) 5250-5255.
[31
Riesemeier, Investigation of water evolution and transport in fuel cells with high resolution synchrotron x-ray radiography, Applied Physics Letters, 90 (2007) 174105.
[32] I.V. Zenyuk, D.Y. Parkinson, G. Hwang, A.Z. Weber, Probing water distribution in compressed fuel-cell gas-diffusion layers using X-ray computed tomography, Electrochemistry Communications, 53 (2015) 24-28.
[33] W.K. Epting, S. Litster, Microscale measurements of oxygen concentration across the thickness of diffusion media in operating polymer electrolyte fuel cells, Journal of Power Sources, 306 (2016) 674-684.
[34] J. Eller, J. Roth, R. Gaudenzi, S. Irvine, F. Marone, M. Stampanoni, A. Wokaun, F.N. Büchi, Water Distribution in GDL near Optimal Humidification, ECS Transactions, 50 (2013) 477-486.
[35] I.V. Zenyuk, E. Medici, J. Allen, A.Z. Weber, Coupling continuum and pore-network models for polymer-electrolyte fuel cells, International Journal of Hydrogen Energy.
[36] C.A. Schneider, W.S. Rasband, K.W. Eliceiri, NIH Image to ImageJ: 25 years of image analysis, Nat Meth, 9 (2012) 671-675.

[37] A. Groso, R. Abela, M. Stampanoni, Implementation of a fast method for high resolutionphase contrast tomography, Optics Express, 14 (2006) 8103-8110.
[38] S.S. Singh, J.J. Williams, P. Hruby, X. Xiao, F. De Carlo, N. Chawla, In situ experimental techniques to study the mechanical behavior of materials using X-ray synchrotron tomography, Integrating Materials and Manufacturing Innovation, 3 (2014) 1-14.
[39] T. Hildebrand, P. Rüegsegger, A new method for the model-independent assessment of thickness in three-dimensional images, Journal of Microscopy, 185 (1997) 67-75.
[40] M. Doube, The Ellipsoid Factor for Quantification of Rods, Plates, and Intermediate Forms in 3D Geometries, Frontiers in Endocrinology, 6 (2015).
[41] M. Doube, M.M. Kłosowski, I. Arganda-Carreras, F.P. Cordelières, R.P. Dougherty, J.S. Jackson, B. Schmid, J.R. Hutchinson, S.J. Shefelbine, BoneJ: Free and extensible bone image analysis in ImageJ, Bone, 47 (2010) 1076-1079.
[42] O.S. Burheim, J.G. Pharoah, H. Lampert, P.J.S. Vie, S. Kjelstrup, Through-Plane Thermal Conductivity of PEMFC Porous Transport Layers, Journal of Fuel Cell Science and Technology, 8 (2010) 021013-021013-021011.
[43] N. Epstein, On tortuosity and the tortuosity factor in flow and diffusion through porous media, Chemical Engineering Science, 44 (1989) 777-779.
[44] A.L. Buck, New Equations for Computing Vapor Pressure and Enhancement Factor, Journal of Applied Meteorology, 20 (1981) 1527-1532.
[45] G. Xu, J.M. LaManna, J.T. Clement, M.M. Mench, Direct measurement of through-plane thermal conductivity of partially saturated fuel cell diffusion media, Journal of Power Sources, 256 (2014) 212-219.

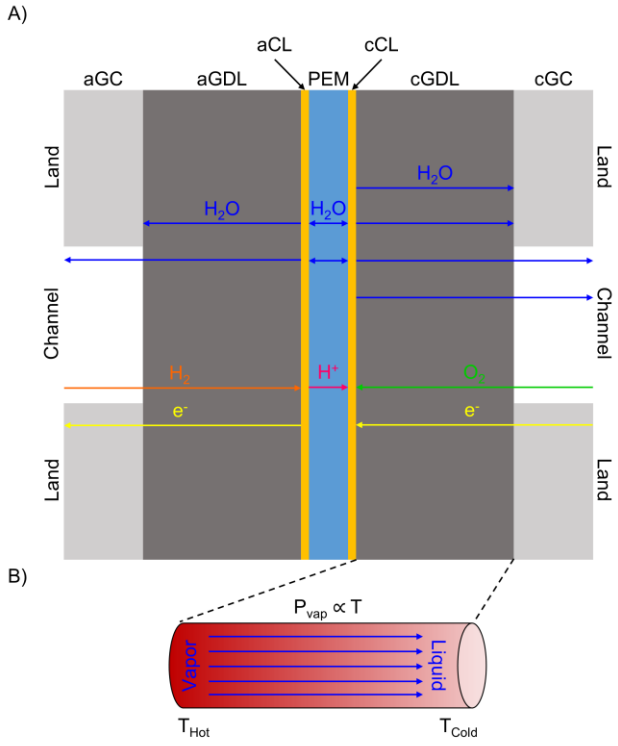

Figure 1. a) Cross-section of PEFC and b) PCI flow schematic with transport processes shown.

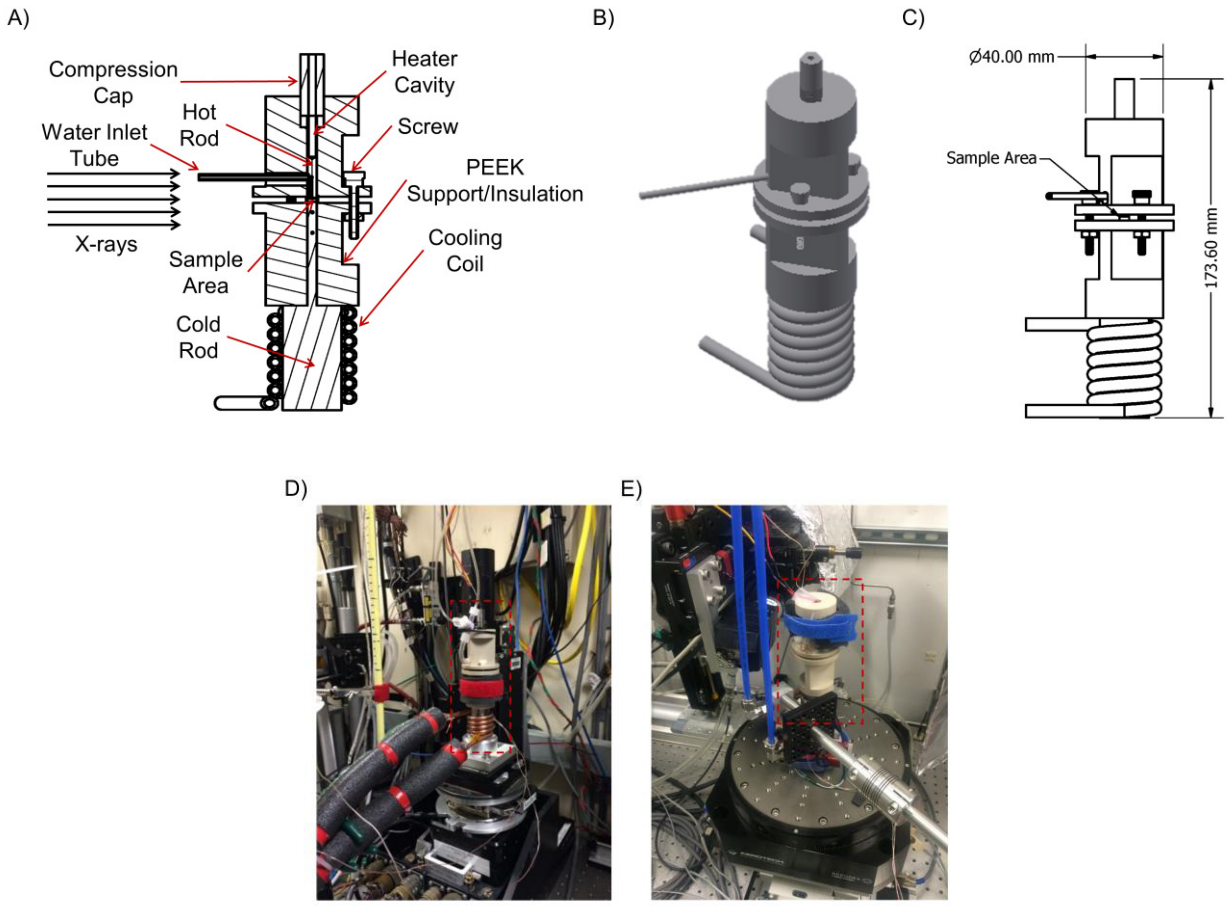

Figure 2. Experimental setup a) computer-aided-design (CAD) cross-section view identifying various components, b) CAD shaded view, c) CAD overall dimensions, d) setup at LBNL ALS Beamline 8.3.2, and e) setup at ANL APS Beamline 2-BM-A.

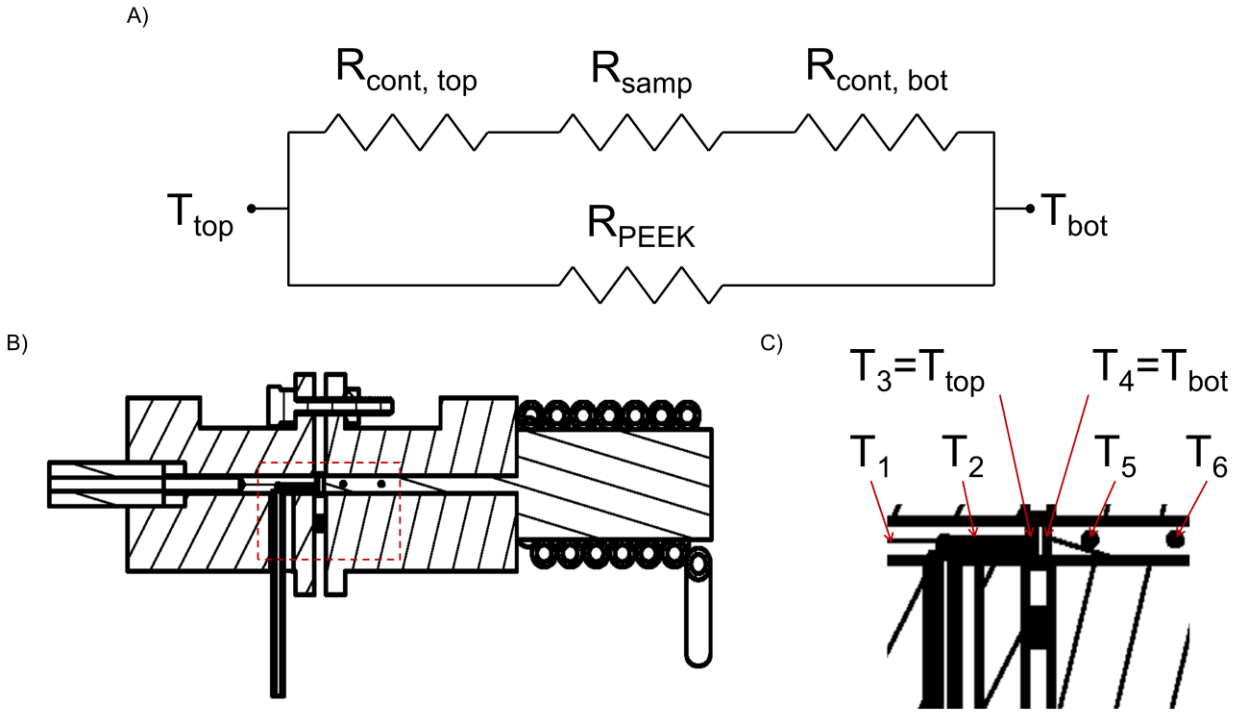

Figure 3. a) Resistance network used to estimate thermal conductivity. b) Rotated apparatus and c) cut-out with temperature locations shown.

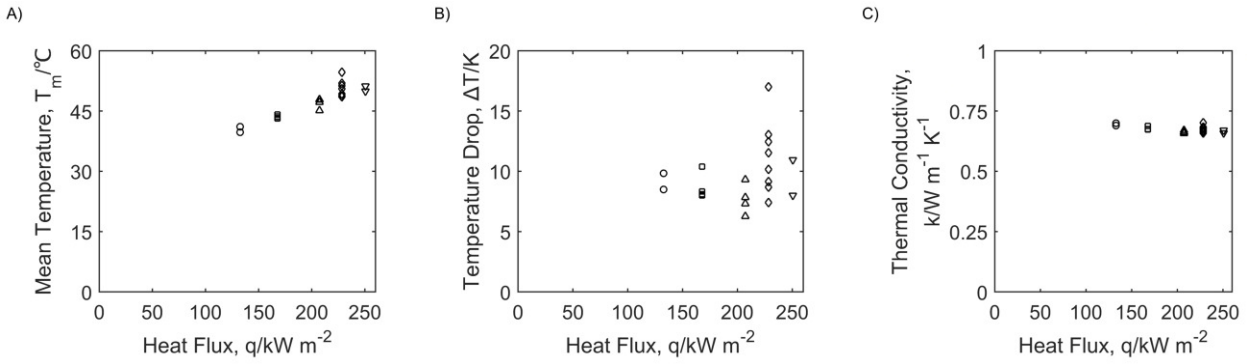

Figure 4. a) Mean temperature, b) temperature drop, and c) thermal conductivity as functions of heat flux, q.

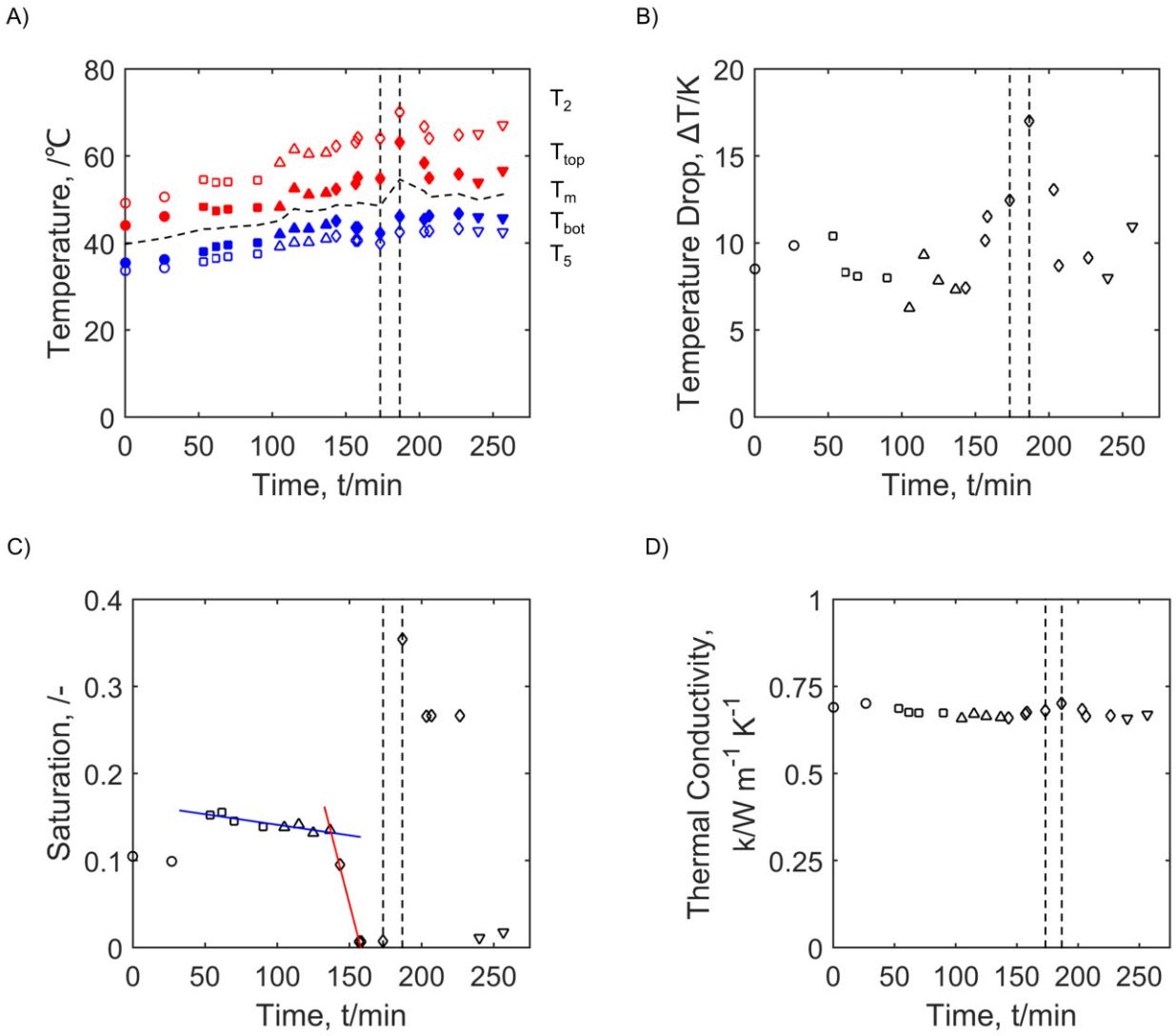

Figure 5. a) Temperature, b) temperature drop, c) saturation, and d) thermal conductivity as functions of time, t. Dashed lines indicate times at which more water was introduced. Marker shapes group data by heat flux (see Figure 4).

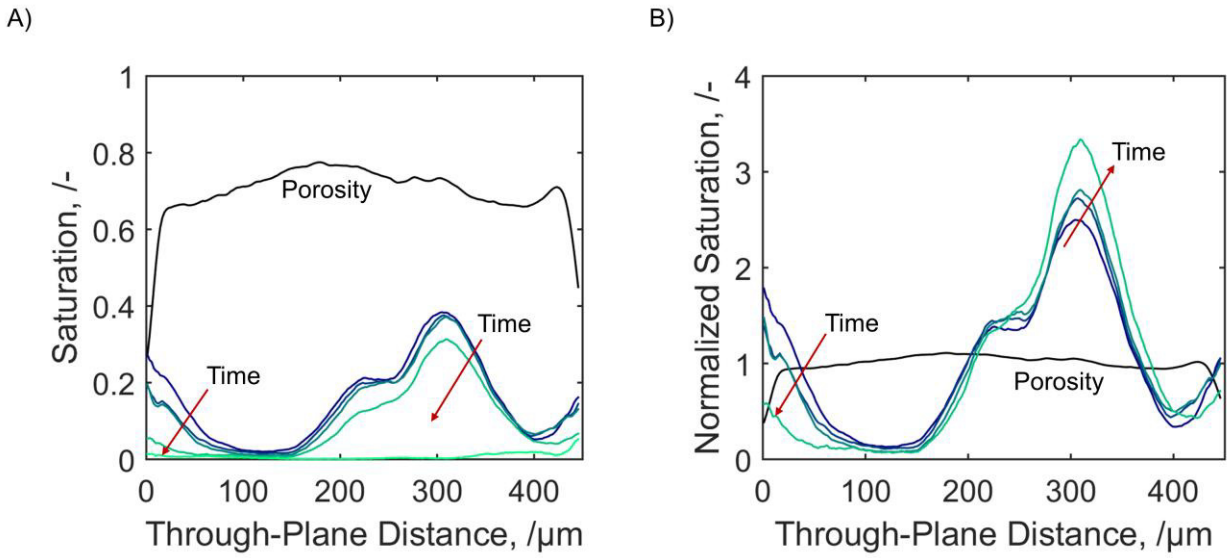

Figure 6. a) Saturation in through-plane direction and b) normalized to individual volume-average saturations. The hot (top) face of the GDL is the origin.

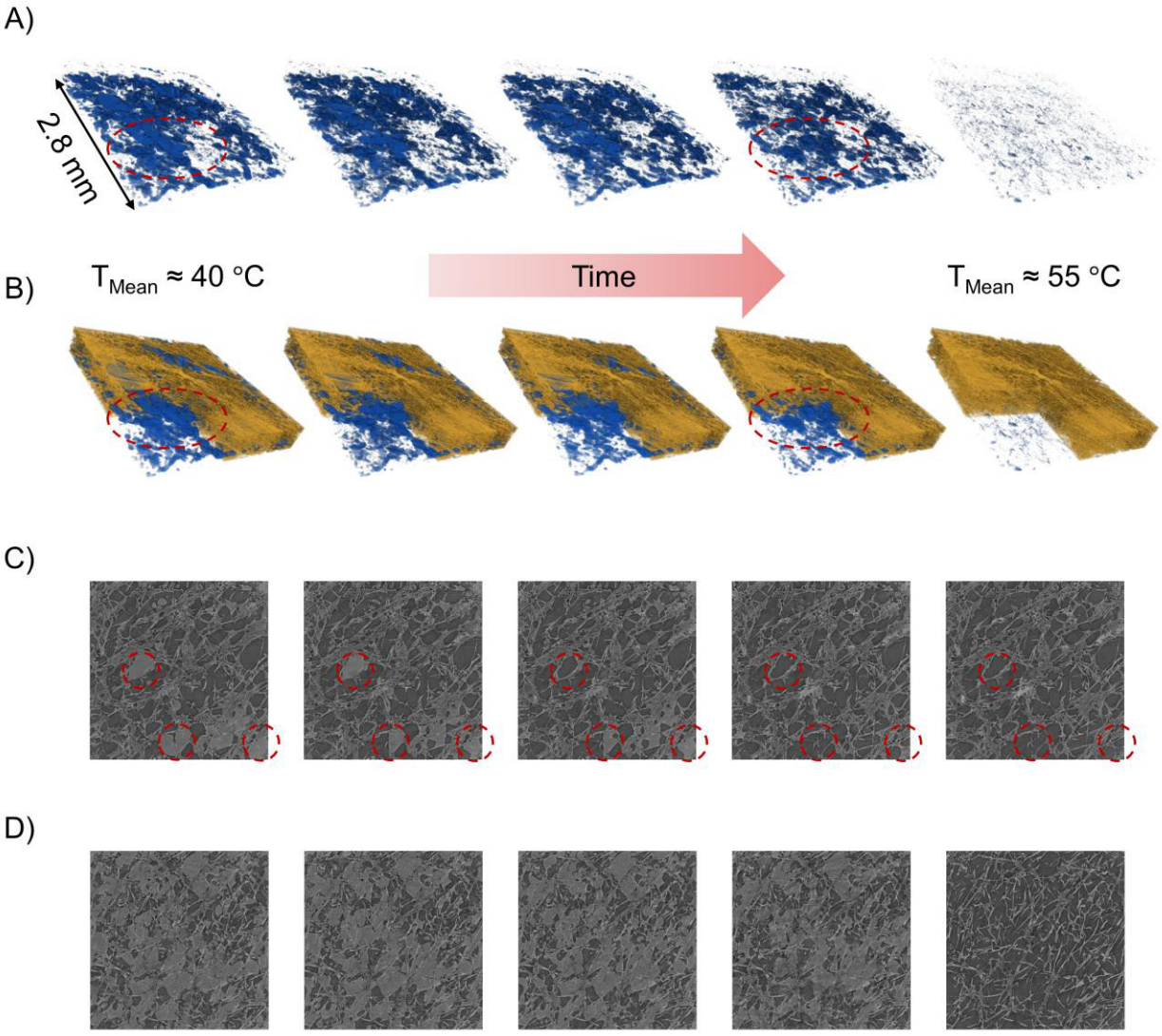

Figure 7. Time series of a) 3D volume-rendered water clusters, b) 3D volume-rendered water clusters with fibers/PTFE, c) gray-scale in-plane cross-section near top, and d) gray-scale in-plane cross-section near bottom.

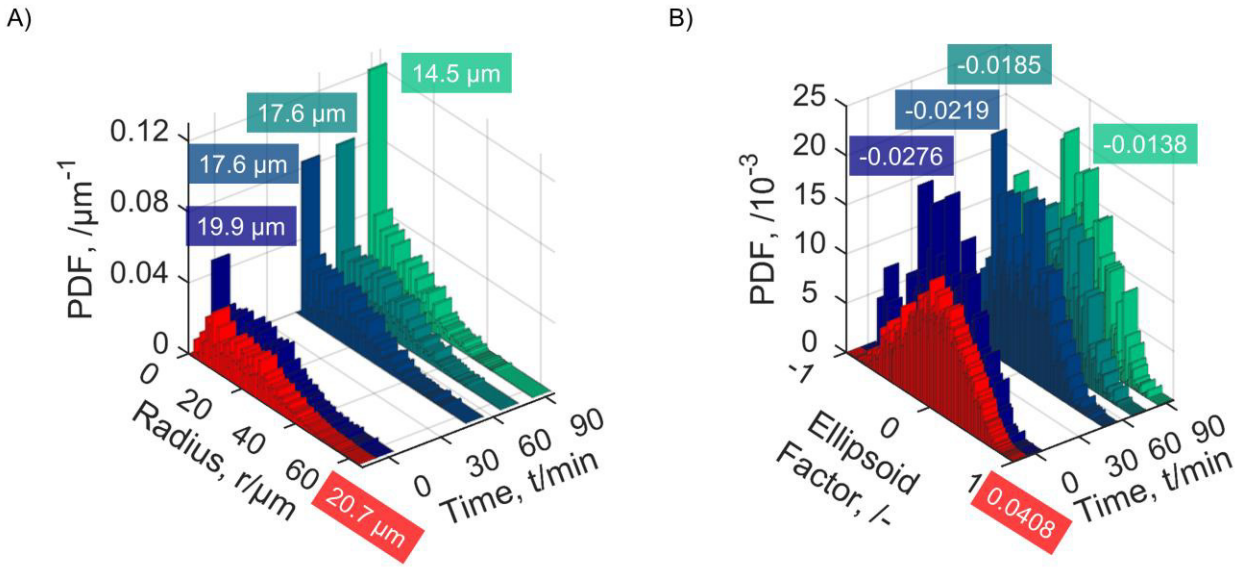

Figure 8. Time series of water cluster a) size distribution and b) ellipsoid-factor (EF) distribution. In both plots, the data set colored red is for the pores of the dry sample. Mean values are labeled for each data set.

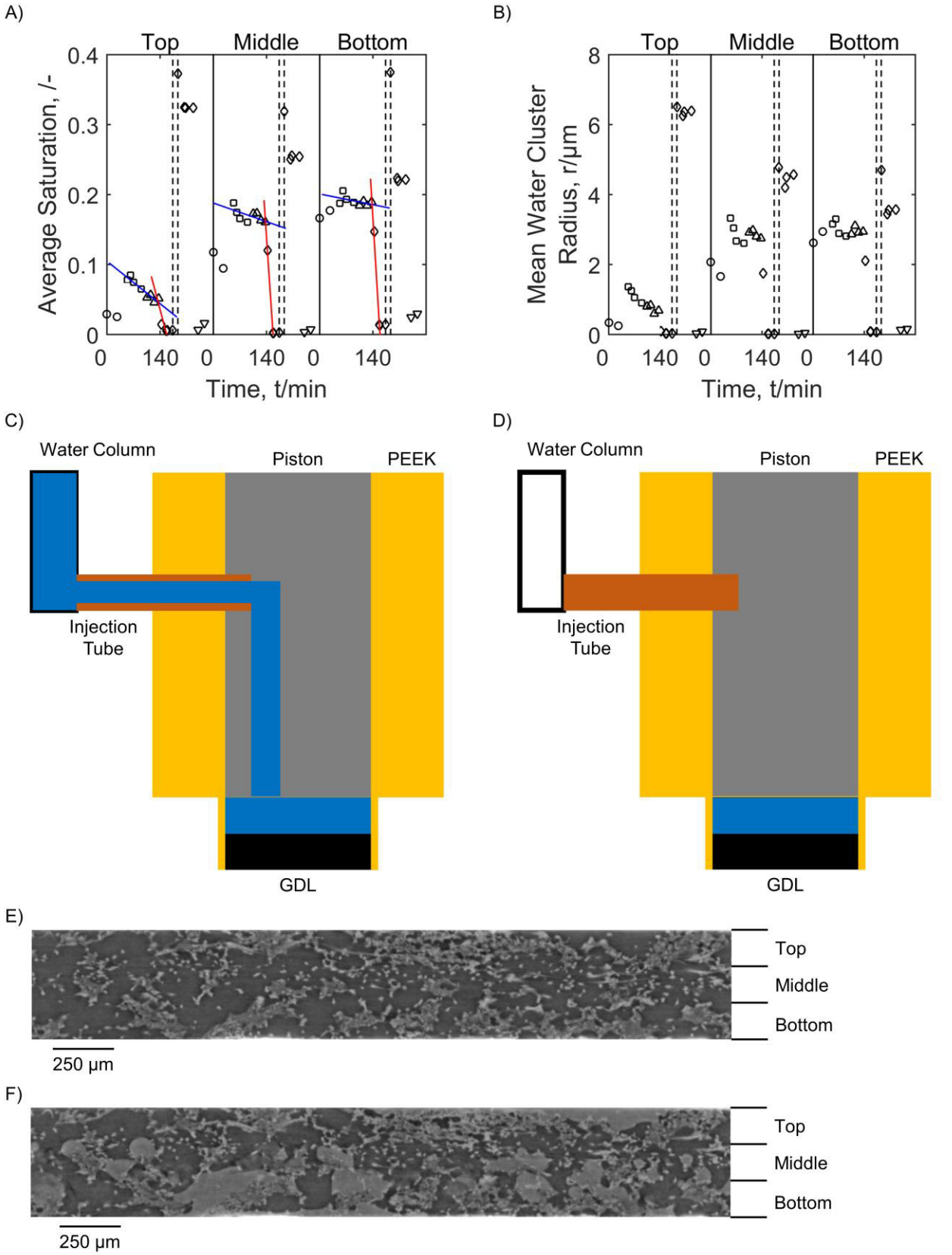
A)
Top
Middle
Bottom
Average Saturation, /-
0.4
0.3
0.2
0.1
0
0
140
0
140
0
140
Time, t/min
B)
Top
Middle
Bottom
Mean Water Cluster Radius, r/µm
8
6
4
2
0
0
140
0
140
0
140
Time, t/min
C)
Water Column
Piston
PEEK
Injection Tube
GDL
D)
Water Column
Piston
PEEK
Injection Tube
GDL
E)
Top
Middle
Bottom
250 µm
F)
Top
Middle
Bottom
250 µm

Figure 9. a) Volume-average saturation with a fit (blue line) indicating evaporation when water reservoir was connected to the sample and a fit (red line) indicating evaporation without water reservoir. b) Mean water cluster size (radius) as a function of time. Data is split into thirds by equal spacing along the through-plane direction. c-d) Show (not to scale) the two different evaporation cases; with and without a water reservoir respectively. e-f) Gray-scale images obtained from reconstructing data for dry and wet samples respectively. These images are labeled to show the top, middle, and bottom regions referred to in a-b.

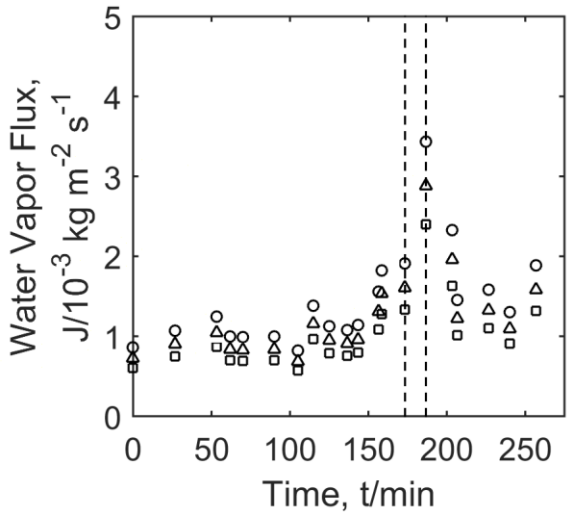

Figure 10. Water vapor flux for the entire GDL, as predicted by Equation (14). Circles correspond to the tortuosity-porosity value provided by [4], triangles correspond to the tortuosity and porosity (ε_1) values provided by [15], and squares correspond to the tortuosity provided by [15] combined with the porosity (ε_2) values determined in this experiment.